Experimental and numerical study of fluidization and pressure drop of spherical and non-spherical particles in a model scale fluidized bed

K. Vollmari [a,*], R. Jasevičius [b,c], H. Kruggel-Emden [a]

[a] Ruhr-Universitaet Bochum, Universitaetsstrasse 150, D-44780 Bochum, Germany
[b] Vilnius Gediminas Technical University, Sauletekio al. 11, LT-10223 Vilnius, Lithuania
[c] Vilnius University, Universiteto g. 3, LT-01513 Vilnius, Lithuania

ABSTRACT

A laboratory scale fluidized bed was examined experimentally and numerically involving differently sized wooden Geldart-D particle shapes. Simulations were performed with a coupled DEM–CFD approach, which involves a drag force model that realizes for the particle shape and orientation. To validate the drag force model and to learn more about the fluidization behavior of non-spherical particles the pressure drop, particle height and orientation distributions were analyzed. To gain comparable data from the experiments, a PTV-MATLAB script was developed to detect particles and determine their orientations and heights. Experimental and numerical results are in good agreement for most particle types; differences in the pressure drop can be allocated to mismatching particle heights or orientations. Differences in the particle height distribution are a result of particles that stack up in corners or close to the vessel walls. It was found that despite these local deviations the DEM–CFD can accurately reproduce the orientation behavior of elongated particles, which with increasing velocity align themselves with the flow. For elongated particles below a certain elongation ratio this behavior could not be observed, which was confirmed by both experiments and simulations.

© 2015 Published by Elsevier B.V.

1. Introduction

Fluidized beds are widely used in mechanical process engineering, energy technology and processing technology and are often attributed to operational problems [1–4]. Some of these problems are directly related to the particle orientation, e.g. segregation of elongated particles from equidimensional particles. To overcome them and to additionally improve product quality or enhance energy efficiency, experimental and numerical investigations are available as viable tools. As experimental investigations are costly at industrial scales and cannot easily be scaled up from laboratory size experiments, the simulation and detailed analysis of fluidized bed processes is not only of academic but also of industrial interest. Furthermore the usually dense two-phase systems in fluidized beds are not easily examined experimentally. Optical approaches like fiber optical probe (FOP), laser Doppler velocimetry (LDV), particle tracking velocimetry (PTV), and particle image velocimetry (PIV) [5] are often limited to the outer planes of a fluidized bed or are invasive; noninvasive techniques for the investigation of the interior of a bed like positron emission particle tracking (PEPT), radioactive particle tracking (RPT), magnetic particle tracking (MPT) or radio-frequency identification (RFID) are whether difficult to

apply or still in development [6,7]. In contrary simulations provide reliable, full access into the fluidized bed if being properly validated, without interrupting the particle motion or flow processes. As fluidized beds are multi-phase systems, approaches that combine two simulation frameworks offer a high level of accuracy. The coupled discrete element method (DEM)–computational fluid dynamics (CFD) approach, which combines discrete particle tracking with a cell-averaged fluid simulation, has proven capable for the simulation of fluidized beds with spherical particles in the past [8–13]. The discrete element method developed in 1979 dates back to Cundall and Strack [14] and since then has been applied in a wide range of fields. The first coupled DEM–CFD simulation to describe a fluidized bed was performed by Tsuji et al. [15] as early as 1993 for a two dimensional system of 2400 spherical particles. With increasing computational power three dimensional systems including up to 4.5 million particles became possible, recently [16]. A comprehensive review of the developments and applications of the DEM for spherical particles was given by Zhu et al. [17, 18]. However, spherical particles are only able to describe real systems, meaning systems that comprise of complex shaped particles, to a limited degree. Large, non-spherical particles are especially of interest for refuse-derived fuel and biomass [19], drying applications [20], food processing [21] and bulk solid handling [22]. Therefore, in recent years the implementation of complex shaped particles gained more and more attention [23–27]. A review on recent developments of the DEM

including the realization of complex shaped particles was given by Lu et al. [28], who consider the particle shape as one of the most important factors to be considered in DEM simulations.

Complex shapes can be expressed through multiple methods including super quadrics, polyhedrons and clustered spheres [26]. The approximation quality can thereby vary from very rough to very fine and will affect the run time of the simulation. Where a compromise between accuracy and speed should be drawn, needs to be examined individually [29]. Polyhedrons are able to represent angular shapes accurately with low polygon counts, while with increasing polygon counts not only model type particles (cubes, cuboids, pyramids, tetrahedrons, etc.), but also real particles with uneven surfaces and edges can be approximated [30]. As fine approximations are difficult to obtain, automated solutions were developed in recent years. Latham et al. [31] presented a method utilizing a 3D laser ranging system to capture irregular geometries into 3D models. Williams et al. [32] developed an image based segmentation technique that is able to acquire particle shapes.

A first contribution to the simulation of two-phase systems involving non-spherical particles was made by Zhong et al. [33], who investigated cylindrical particles approximated through clustered spheres with the DEM–CFD utilizing the drag force model by Tran Cong et al. [34] during dilute flow in a fluidized bed. However, this approach is not suitable for dense particle systems as the influence of the void fraction is not appropriately considered. Recently an improved and very versatile drag force model for single, complex shaped particles was proposed by Hölzer and Sommerfeld [35]. This model in combination with a model for the representation of the void fraction by Di Felice [36] has been used in many recent DEM–CFD-studies addressing complex shaped particles such as in the investigation by Hilton et al. [37], who simulated a fluidized bed involving four types of complex shaped particles, expressed through super quadrics. A modification of the model by Di Felice [36] was proposed by Rong et al. [38]. Results obtained by Hilton et al. [37] showed that in fluidized systems the particle shape has a strong influence on the pressure drop and traditional correlations like the Ergun-equation [39] were not able to correctly reproduce this. A similar modeling approach to [37] was chosen by Zhou et al. [40] who simulated ellipsoidal and oblate particles and who thereby confirmed that the general flow behaviors of the examined particles could be reflected through the DEM–CFD. Corn-shaped particles consisting of clustered spheres were examined by Ren et al. [41,42] in a spouted bed. They examined the approximation quality of particles clustered with different accuracy. Oschmann et al. [43] compared among other shapes ideal cylinders approximated by either polyhedrons or clustered spheres and found a faster mixing rate for clustered particles. Other gas–solid systems that have been examined by the DEM–CFD include pneumatic conveying [44,45] and fixed beds [46].

So far obtained numerical and experimental results indicate that in fluidized systems that involve complex shaped particles the particle orientation is an important factor that influences the process quality [47,48] and the fluidization behavior [43,49] and should therefore be analyzed further. Image analysis of fluidized beds has been widely used to examine voids and bubbles [50,51] and particle velocities on the basis of the particle tracking velocimetry (PTV) [52]; PTV can also be used to study the orientations of particles. Experimental investigations of the orientation distributions of cylinders and cubes in pipe flow have been performed by Zitoun et al. [53] and numerical investigations by Ku and Lin [54] and Zhang et al. [55]. The orientations of cylindrical particles with different elongation ratios were examined numerically and experimentally by Cai et al. [56] in fluidized beds. The tendency of elongated particles to align themselves with the flow was confirmed in all three studies. In the DEM particle orientations are crucial for the contact detection and determination of the rotational movement. Furthermore local porosities can vary depending on the particle orientation, so that a fixed bed of equal overall porosity involving complex shaped particles behaves differently than a packing consisting of spheres [46].

To test the validity of the DEM–CFD to precisely predict particle orientations, to gain further knowledge about the particle shape

influence on particle orientation in gas–solid flows and to further validate the applicability of the implemented DEM–CFD submodels for the drag force calculation [35,36], a comparative experimental and numerical study with a fluidized bed operated with 13 differently sized and shaped particle classes is carried out. A particle tracking script was derived and validated to perform PTV. It is implemented in Matlab and allows detecting particle positions and orientations of selected particles in the experiments. Based on this, a comparison with DEM–CFD simulation is possible, where particle positions and orientations are inherently available over time.

2. Methodology

2.1. DEM–CFD approach for the simulation of fluidized beds

In this study an Eulerian–Lagrangian approach was used to describe the fluidized system. Hereby particles are tracked discretely, while the fluid phase is modeled as a continuum by solving the volume averaged Navier–Stokes equations [17]. In the DEM the translational and rotational motion is obtained by integrating Newton's and Euler's equations of each particle given by

$$m_i \frac{d^2 \vec{x}_i}{dt^2} = \vec{F}_i^c + \vec{F}_i^{pf} + m_i \vec{g}, \tag{1}$$

$$\hat{I}_i \frac{d\vec{W}_i}{dt} + \vec{W}_i \times \left(\hat{I}_i \vec{W}_i \right) = \Lambda_i^{-1} \vec{M}_i, \tag{2}$$

with the particle mass m_i, particle acceleration $d^2 \vec{x}_i/dt^2$, contact force $\vec{F}_i^c$, particle/fluid force $\vec{F}_i^{pf}$, gravitational force $m_i \vec{g}$, angular acceleration $d\vec{W}_i/dt$, angular velocity $\vec{W}_i$, external moment resulting out of contact or particle/fluid forces $\vec{M}_i$, the inertia tensor along the principal axis $\hat{I}_i$ and the rotation matrix converting a vector from the inertial into the body fixed frame Λ_i^{-1}.

Complex shaped particles are modeled through the polyhedron method, which allows to precisely reproduce angular shapes by compositing triangles. The triangular surface mesh that represents the particle makes it necessary to adjust the contact detection model, so that a common plane algorithm [26] is used as a basis. Contact force laws are applied similarly as used for spherical particles [57,58]. A linear spring damper model is used to provide the normal component of the contact forces

$$\vec{F}^n = k^n \delta \vec{n} + \gamma^n \vec{v}_{rel}^n, \tag{3}$$

where k^n is the spring stiffness, δ the virtual overlap, $\vec{n}$ a normal vector, γ^n a damping coefficient and $\vec{v}_{rel}^n$ the normal velocity in the contact point. Both k^n and γ^n determine the coefficient of normal restitution between particles e_{PP}^n as well as particles and walls e_{PW}^n. For the calculation of the tangential forces a linear spring limited by the Coulomb condition is used

$$\vec{F}^t = min\left(k^t \left| \vec{\xi} \right|, \mu_C \left| \vec{F}^n \right| \right) \cdot \vec{t}, \tag{4}$$

where k^t is the stiffness of a linear spring, μ_C is the friction coefficient, $\vec{\xi}$ is the relative tangential displacement and $\vec{t}$ is the tangential unit vector. No rotational friction is considered.

Computational fluid dynamics (CFD) in an Eulerian framework is used to describe the fluid phase. Hereby the inside of the fluidized vessel is meshed with a hexagonal Cartesian grid. The fluid velocity is then addressed as a spatially averaged quantity in each cell. The fluid properties and velocity vector of each cell is then passed on to the DEM through the CFD-framework. The equation of continuity (Eq. (5)) and

the equation of momentum (Eq. (6)) are solved

$$\frac{\partial\left(\varepsilon_f\rho_f\right)}{\partial t} + \nabla\left(\varepsilon_f\rho_f\,\vec{u}\right) = 0, \tag{5}$$

$$\frac{\partial\left(\varepsilon_f\rho_f\,\vec{u}\right)}{\partial t} + \nabla\left(\varepsilon_f\rho_f\,\vec{u}\,\vec{u}\right) = -\varepsilon_f\nabla p + \nabla\left(\overline{\overline{\varepsilon_f\tau}}\right) + \varepsilon_f\rho_f\,\vec{g} + \vec{f}_{int}, \tag{6}$$

where $\vec{u}_f$, ρ_f and p are the physical fluid velocity, density and pressure. $\vec{f}_{int}$ is the volumetric particle/fluid interaction applied in each CFD cell, ε_f is the local fluid porosity and $\overline{\overline{\tau}}$ is the fluid viscous stress tensor $\overline{\overline{\tau}} = \eta_e[(\nabla\vec{u}_f) + (\nabla\vec{u}_f)^{-1}]$ with η_e the effective viscosity determined from the standard k-ε turbulence model. The particle/fluid interaction $\vec{f}_{int}$ is given component wise as $f_{int_i} = \beta_i(u_i - v_i)$, where v_i is the fluid cell averaged particle velocity and β_i is the fluid cell averaged particle/fluid friction coefficient with $i = x, y, z$.

The particle/fluid force $\vec{F}_i^{pf}$ consists of all individual particle/fluid forces including the drag force $\vec{F}_i^d$ and pressure gradient force $\vec{F}_i^{\nabla p}$ acting on a particle i written as $\vec{F}_i^{pf} = \vec{F}_i^d + \vec{F}_i^{\nabla p}$. Both can be combined to $\vec{F}_i^d + \vec{F}_i^{\nabla p} = \vec{\beta}_iV_i(\vec{u}_f - \vec{v}_i)/(\varepsilon_f(1 - \varepsilon_f))$, where V_i is the particle volume. For the calculation of the drag force $\vec{F}_i^d$ and the combined drag and pressure gradient force $\vec{F}_i^d + \vec{F}_i^{\nabla p}$ various models are available. Some approaches are only capable of the description of spherical particles, while the approach by Di Felice [36], where the force for an isolated spherical particle is calculated and altered by the influence of surrounding particles is also suitable for non-spherical particles. Note, that other models are also available for realizing the particle system influence [38] which are however not used here. The respective resulting combined drag and pressure gradient force reads

$$\vec{F}_i^{pf} = \vec{F}_i^d + \vec{F}_i^{\nabla p} = \frac{1}{2}\rho_f\,|\vec{u}_f - \vec{v}_i|C_DA_\perp\varepsilon_f^{1-\chi}\left(\vec{u}_f - \vec{v}_i\right) \tag{7}$$

where C_D is the drag coefficient, $A_\perp$ is the cross-sectional area perpendicular to the flow and χ a correction factor. Eq. (7) can be re-written in terms of the particle/fluid friction coefficient as.

$$\vec{\beta}_i = \frac{1}{2}\rho_fC_DA_\perp\varepsilon_f|\vec{u}_f - \vec{v}_i|(1 - \varepsilon_f)\frac{1}{V_i}\varepsilon_f^{(1-\chi)}. \tag{8}$$

χ is calculated as a function of the particle Reynolds-number $Re = \varepsilon_f\rho_fd_e|\vec{u}_f - \vec{v}_i|/\eta_f$ as

$$\chi = 3.7 - 0.65\exp\left(-(1.5 - \log(Re))^2/2\right) \tag{9}$$

with $d_e = (\frac{6}{\pi}V_p)^{1/3}$ the diameter of a volume equivalent spherical particle and η_f the fluid viscosity. The drag coefficient C_D of a single particle (spherical or non-spherical) can be derived from correlations such as Hölzer und Sommerfeld [35] which can be written as

$$C_D = \frac{8}{Re}\frac{1}{\sqrt{\phi_\perp}} + \frac{16}{Re}\frac{1}{\sqrt{\phi}} + \frac{3}{\sqrt{Re}}\frac{1}{\phi^{3/4}} + 0.42 \times 10^{0.4(-\log(\phi))^{0.2}}\frac{1}{\phi_\perp} \tag{10}$$

where $\phi_\perp$ is the crosswise sphericity which is the ratio between the cross-sectional area of the volume equivalent sphere and the projected cross-sectional area of the considered particle perpendicular to the flow. Therefore, the particle orientation is directly considered through the crosswise sphericity in the calculation of the drag coefficient. For spherical particles the cross-sectional area $A_\perp$ perpendicular to the flow required for Eqs. (7) and (8) and the crosswise sphericity $\phi_\perp$ needed

for Eq. (10) can be readily calculated. As these calculations require iterative procedures to determine the cross-sectional area for polyhedra, which represent the complex shaped particles in this study, $A_\perp$ is calculated in advance for every particle shape and provided to the DEM for faster calculation times. The data is stored in dependence on three symmetric Euler parameters and the sign of the fourth parameter [43]. The porosity of each CFD-cell is calculated with a subgrid cell approach. A higher resolved second grid is layed upon the CFD-grid, which is then examined to identify if a particular subgrid cell center lies within a particle. If this is the case the respective subcell is considered as fully filled with solid. The fluid porosity is then calculated based on the obtained ratio [43].

2.2. Image analysis

In simulations of non-spherical particles with the coupled DEM–CFD approach the orientation is an important parameter. It is considered through the projection area $A_\perp$ in Eqs. (7) and (8) and the crosswise sphericity $\phi_\perp$ in Eq. (10) and therefore directly related to the pressure drop of the system through the volumetric particle/fluid interaction $\vec{f}_{int}$. The orientations of particles in a DEM–CFD simulation can be readily determined as every particle is tracked individually and the coordinates and orientations are continuously monitored. A direct comparison between the particle orientations of the experiments and simulations is important for a better understanding of the fluidization and pressure drop behavior of a fluidized bed. But the effort to determine particle orientations in the experiments is substantially higher compared to the simulations. The simplest approach would be to manually determine the orientation of each particle in an obtained picture of a fluidized bed such as in Fig. 1 (1). As a reasonable long timespan at a high enough frequency of images should be analyzed to get a representative overview over the state of the fluidized bed, it is impossible to do so manually within a justifiable amount of time. Therefore, an automated solution is needed to detect particles and determine their orientation. In the course of this study an image detection was developed as part of a PTV approach in Matlab that is able to process images of equidimensional and elongated particles. In Fig. 1 the sequence of the image detection is outlined.

As the observed fluidized bed is a highly dense system and particles are in frequent contact, a method was implemented to isolate the particles from each other for a better recognition. The input (1) is given by a RGB-image of the fluidized bed, which is then cropped to the region of interest. Particle dimensions are determined with the Matlab distance tool for later use [59]. Furthermore to eliminate interferences by scratches or staining of the freeboard region, an initial picture is determined and then subtracted from the current picture. As the black background has color value in the HSV space of (0|0|0) only areas that differ from this value, which therefore are non-black because of interferences, are affected by this subtraction. After these initial steps, edges of the input image are detected (2a) by the use of the Canny algorithm [60]. The edge image of the particles can then be subtracted from the initial image to remove a thin outer layer around every particle and thus isolate the particles from each other for the further analysis. As the boundaries of an individual particle in the binary edge image (2b) may not be completely connected to each other, a multitude of morphological operations like dilatation and closing are performed to close existing gaps. The resulting image (2c) is then subtracted from a binary image calculated from the initial RGB-image. This way the particles that before were touching each other are separated and ready for the particle detection through a blob analysis (4). The blob analysis [61] finds connected pixels by checking the neighborhood of every pixel and thus is able to detect the isolated particles. As sometimes two or more particles can still be connected to each other, a threshold criterion is applied. The threshold is calculated from the particle dimensions that are measured at the beginning of the process. Areas where connected
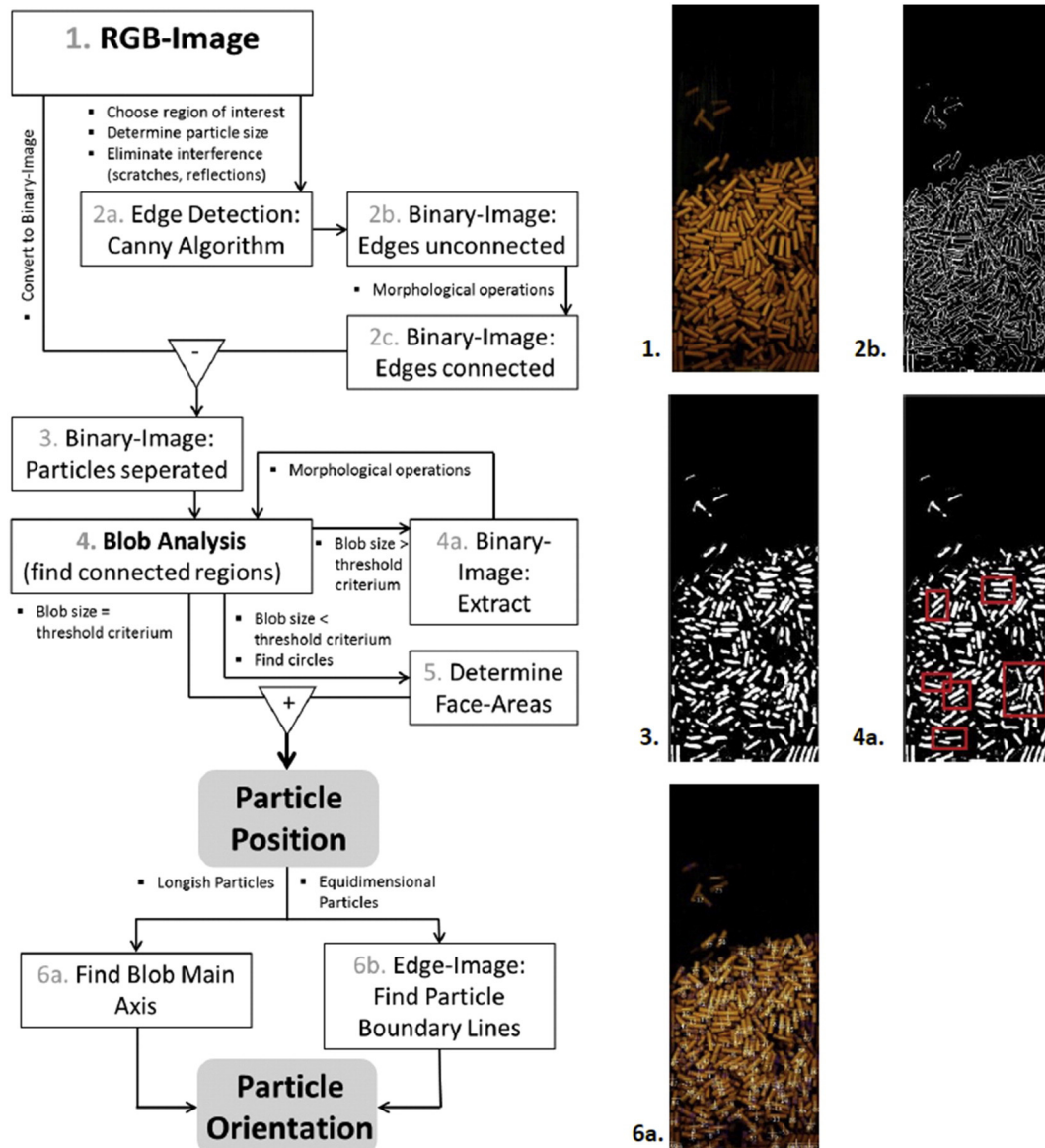
Fig. 1. Sequence of the image analysis to detect particle positions and orientations (left) and selected corresponding images (right).

pixels are found that surmount the criterion are then again processed with a set of morphological operations to separate eventually connected particles (4a). Areas with less connected pixels than the criterion are accepted as face areas (5). In the case of cylinders, the face area is of circular shape and can therefore be identified through a Hough transformation [62]. Connected regions that fulfill the threshold criterion are marked as sidewards facing particles. The combination of the side areas and face areas then gives the particle positions. Based on these positions, the orientation of sidewards facing particles is determined by either calculating the orientation of the main axis for longish particles (6a) or determining the angle of close, parallel edge lines around the particle center for equidimensional particles. To increase the accuracy of the detection method for equidimensional particles, the detected line pairs are evaluated in four terms including the distance from the centroid, difference in length, parallelism and the alignment of the line center to the particle center. The line pair with the best results in these four categories is then chosen to represent the particle orientation.

Note that only the orientation of the pitch axis of a particle can be determined, while rotations among the yaw and roll axis cannot be detected. As the systems that are examined in this study are very dense it can be assumed with good approximation that particles that are visible

through the front plane of the vessel are also aligned parallel towards it, so that no significant error is introduced by analyzing the projection only.

3. Experimental and numerical setup

The experimental examinations are carried out in a laboratory scale fluidized bed made from antistatic polycarbonate with the dimensions width = depth = 0.11 m and height = 0.41 m, displayed in Fig. 2. Particles are placed on a porous plate with an open area of 37% installed at the bottom of the bed. A fully-developed flow profile is ensured by a number of flow straighteners placed bellow the porous plate. A pressure transducer (Newport Omega PD41X-V-50 mbar) is connected to two pressure tapping points installed at h = 0.31 m and below the porous plate at h = −0.02 m.

The measured differential pressure is recorded at a frequency of 250 Hz and later in the analysis reduced by the pressure drop caused by the porous plate. Video footage was created with a high speed digital camera (Optronis CL600x2) at 250 frames per second over a time period of 10–15 s. Through an external clock source pressure and image acquisition are synchronized and can be started simultaneously with a TTL
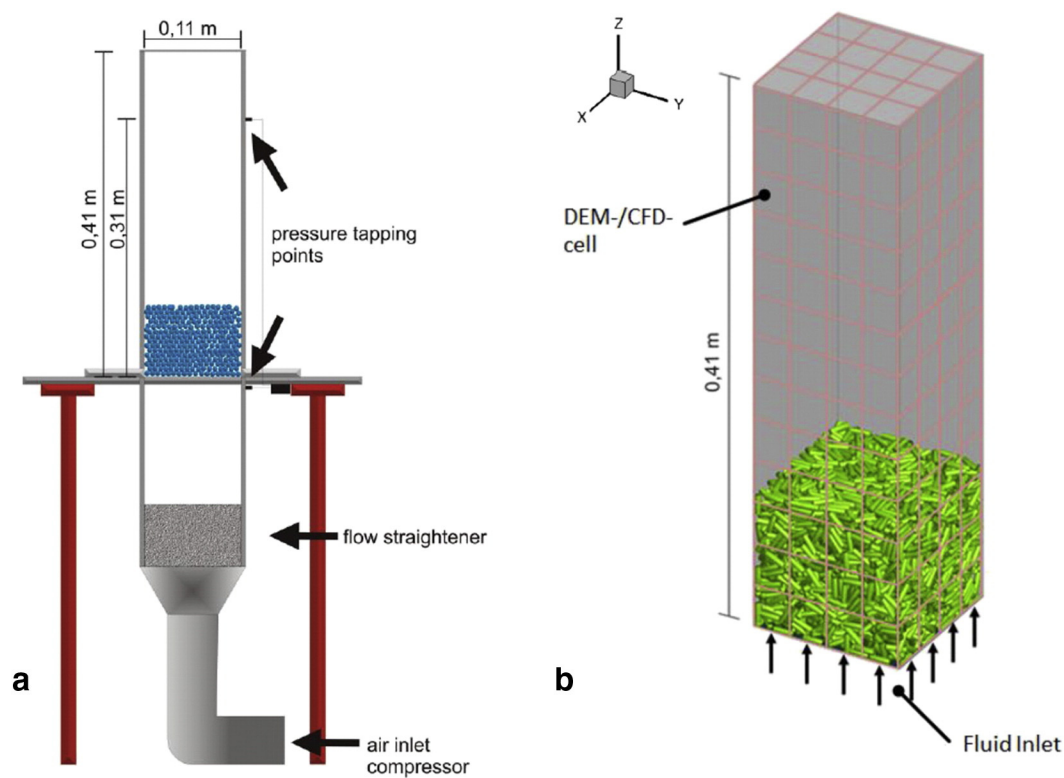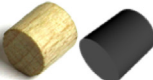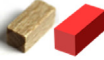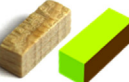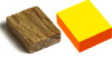
Fig. 2. Experimental (a) and numerical (b) setup and its division into a number of DEM–CFD cells larger than the particle size.

Table 1
Particle properties including the volume equivalent diameter d_{e}-class, the particle dimensions, the sphericity ϕ, the particle density ρ_p, the bed height L and the averaged porosity ε for the initial, unfluidized setup.
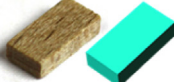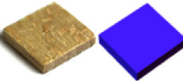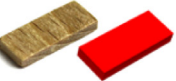
Shape	Sphere	Sphere	Ideal Cylinder	Cube	Cube
d_{e}–class [mm]	7	5	7	5	7
Size [mm]	7.2	5	6.1 6.2	4.2 4.3 4.5	5.2 6.3 6.3
ϕ [–]	1.00	1.00	0.87	0.81	0.80
ρ_p [kg/m³]	772.5	823.0	708.5	639.7	746.9
L_{fb} [mm] / $\bar{\varepsilon}$ [–]	95 0.40	88 0.40	98 0.36	98 0.37	103 0.43
Shape	Elongated Cylinder	Elongated Cuboid	Elongated Cuboid	Plate	Elongated Plate
d_{e}–class [mm]	7	5	7	5	5
Size [mm]	3.9 14.0	3.0 3.0 7.1	4.2 4.2 11.4	2.0 4.9 6.0	2.0 4.0 8.0
ϕ [–]	0.75	0.75	0.73	0.71	0.69
ρ_p [kg/m³]	764.4	745.6	639.7	754.1	756.6
L_{fb} [mm] / $\bar{\varepsilon}$ [–]	103 0.44	103 0.42	115 0.40	102 0.43	108 0.46
Shape	Elongated Cuboid	Plate	Elongated Plate		
d_{e}–class [mm]	5	7	7		
Size [mm]	2.0 3.0 11.0	2.2 9.0 9.8	2.0 6.0 14.9		
ϕ [–]	0.64	0.63	0.58		
ρ_p [kg/m³]	728.1	672.8	721.7		
L_{fb} [mm] / $\bar{\varepsilon}$ [–]	117 0.48	121 0.46	124 0.51		

Table 2
Parameters required for the simulations in accordance to the experimental values.

Property	Abbreviation	Value
Ambient pressure	p_A	101,325 Pa
Specific gas constant air	Rs	287.058 J/kg·K
Ambient temperature	T_A	291.15 K
Gas viscosity	η_f	$1.8302E-05$ kg/m·s
Total particle mass	m_t	0.535 kg

trigger signal. The mass flow rate and superficial velocity are determined in a measuring track with an orifice disk. Geldart-D type beech wood particles of spherical, cylindrical or cuboidal shape are used in all experiments. The combination of beech wood and the antistatic polycarbonate of the vessel ensures that no electrostatic effects disturb the experiments. Attrition or breakage do not occur.

A constant mass of m = 0.535 kg is maintained in all experiments; exact particle parameters are given in Table 1. Corresponding to the equivalent surface sphere diameter d_e particles can be grouped into column to particle diameter ratios of $D/d_e = 15$ for $d_e = 7$ mm and $D/d_e = 22$ for $d_e = 5$ mm classes. The superficial velocity has been increased in steps of 0.1 m/s starting at 0.4 m/s up to 2.4 m/s for all particles.

The numerical setup was modeled on the basis of the experimental setup so that all dimensions and operation conditions are equal. Complex shaped particles like cylinders and cuboids are represented through a polyhedron approximation [26], thus cuboids have the exact same shape and volume as the particles from the experiment while the cylinder shape was closely approximated with 16 edges. Through adjusting the cylinder radius equal volume was maintained. The packings have been generated by dropping randomly oriented particles into the vessel equally distributed over the cross section from a height equal to the height of the vessel. Packing generation procedures equal in experiment and simulation.

The friction and restitution coefficients are determined according to procedures described by Höhner et al. [26] and Hold [63] on the single particle level, respectively. Spring stiffness and damping coefficient determine the maximum overlap for the particle collision. Kruggel–Emden et al. [64] suggested a maximum overlap of 1% of the particle diameter to avoid alteration of the simulations. The coefficients of normal restitution between particles e_{PP}^n and particles and walls e_{PW}^n and the Coulomb friction coefficient μ_C between particles and particles as well as between particles and walls are adjusted to: $e_{PP}^n = 0.5$, $e_{PW}^n = 0.5$, $\mu_{C\_PP} = 0.4$, $\mu_{C\_PW} = 0.3$. The CFD time step is $1 \cdot 10^{-4}$ s; the DEM time step is $1 \cdot 10^{-6}$ s. The stiffness k^n and k^t are calculated so that the maximum overlap condition is fulfilled. A velocity inlet was used as the inflow condition; a pressure outlet as the outflow. The walls were realized with a no-slip boundary condition. Cell sizes in the DEM–CFD simulations (compare Fig. 1b) are $1.833 \times 1.833 \times 1.833$ cm³ in case of $D/d_e = 15$ and $1.375 \times 1.375 \times 1.375$ cm³ for $D/d_e = 22$. The ambient conditions required the DEM–CFD are chosen to be in good agreement with the experimental conditions and are listed in Table 2.

4. Results and discussion

4.1. Validation of the image analysis

In a first step the reliability of the PTV image analysis is examined. Therefore, particle positions and orientations detected with the Matlab-script are compared to manually, in Inkscape, determined values [65]. To achieve equal conditions, the same images, including a fixed bed and a bed in fluidized state are analyzed in both cases. In Fig. 3 particle height distributions are given for four different particle types including equidimensional and elongated cuboids and cylinders. To determine the particle positions manually, the center of every

particle is marked carefully and the coordinates noted down. A frequency distribution is then calculated; particles are grouped into 30 classes depending on their height from 0 to 30 cm.

Results for elongated cylinders with the dimensions d = 4 mm and l = 14 mm are displayed in Fig. 3a. Both methods are in good agreement with average relative deviations of $\delta_x \approx 15\%$. The topmost layer is detected with the highest accuracy in the automated setup, as the bed is more dilute in this case and particles can be easier separated by the automated image detection.

The particle height distribution for 4 mm × 4 mm × 11 mm elongated cuboids is shown in Fig. 3b. The automated method is able to get a good approximation of the particle heights with an average relative deviation of $\delta_x \approx 14\%$ for the fixed bed and $\delta_x \approx 16\%$ for the fluidized bed. Analogously, the results for the 5 mm × 6 mm × 6 mm cubes are displayed in Fig. 3c. The automated detection is able to reproduce the exact, manually determined distribution well with an average deviation of $\delta_x \approx 14\%$ for the fixed bed and $\delta_x \approx 12\%$ for the fluidized bed. As the cuboids have no side or face area, the orientation can be determined for every particle that has been detected. The last particle type that is examined are ideal cylinders with a length and width of 6 mm, shown in Fig. 3d. Overall good agreement between the two identification methods can be observed, with an exact reproduction of the results for the topmost particles. The average deviations amount to $\delta_x \approx 11\%$ for the fixed bed. The quantitative comparison of all cases shows that three different main errors can occur. Particles that are not detected, particles that are detected but the center is out of alignment and falsely recognized particles. Error number two is mostly associated to elongated particles, while error number one is predominantly encountered for cuboids, as these can form stacks which make it hard to find edges for the image detection.

Besides particle positions, the developed PTV Matlab-script is also able to detect orientations of the particles from −89° to 90°. As the angles of −90° and 90° describe the same orientation and without an additional identification mark cannot be distinguished in the experiments, these cases are treated as 90° only. 0° corresponds to a particles that is horizontally aligned with the flow, while −90° and 90° describe particles that are vertically aligned to the flow. The detected orientations are classified with a "less" or "equal to" criterion into groups of 10° for the analysis. For the manual detection of the particle orientations, a line was carefully plotted parallel to the main axis of every particle in Inkscape. In Fig. 4 frequency distributions of the determined particle orientations over the x-z plane for four different particle types are given, with the results for both methods in the case of elongated cylinders with the dimensions 4 mm × 14 mm presented in Fig. 4a. Good overall agreement between both methods can be observed. A deviation in the 85° class is caused by an accumulation of particles parallel to the wall in one corner for the fixed bed, which are not completely automatically detected as a consequence. Similar behavior can be observed for elongated 4 mm × 4 mm × 11 mm cuboids which are shown in Fig. 4b, as these particles show the same tendency to accumulate in chunks with the same orientation. Good agreement between both methods can be observed otherwise.

The orientation determination of equidimensional particles relies on a self-developed algorithm that matches the orientations of detected particle edges to the particle orientation. To validate this method two different equidimensional particles haven been examined. In Fig. 4c results for ideal 6 mm × 6 mm cylinders are shown. As the determination of the orientation is more complicated than for elongated fiber type particles, orientations were only analyzed from 0 to 90°. The ideal cylinders show a generally good agreement between the automated and the manual detection; only for 0° and 90° orientations the automated method detects fewer particles. This is caused by the same problem that occurred for the elongated particles, where particles stacked up in the corners and aligned themselves so that the edge detection cannot clearly identify the particle boundaries.

a)

b)

c)

d)
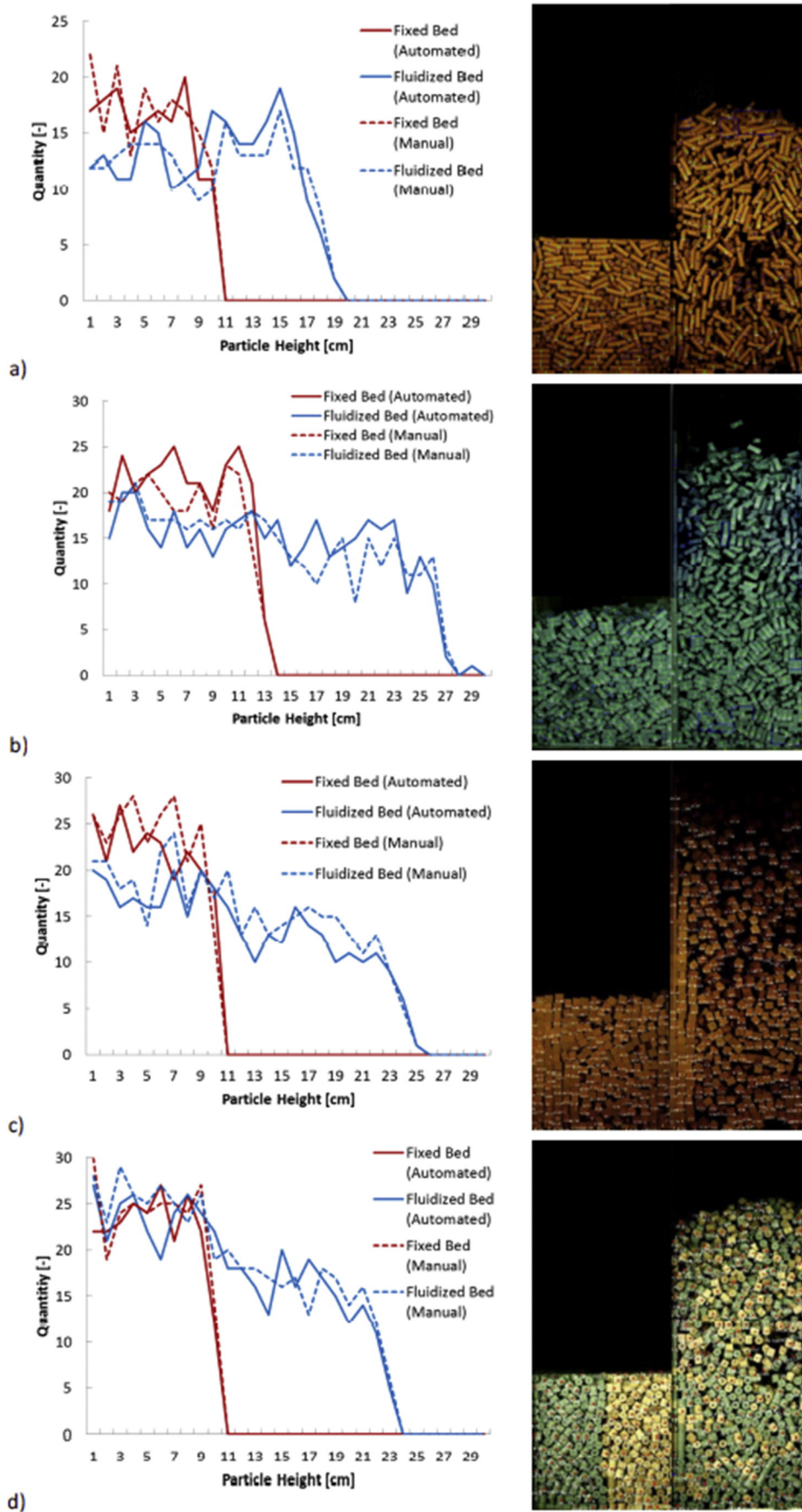
The results for 5 mm × 6 mm × 6 mm cubes are displayed in Fig. 4d, the edge of the cube that lies in the range of 0–90° is hereby considered for the analysis. The deviation in the 50° class can be explained by the false detection of edges caused by wood grains especially in the fixed bed case. This caused an increased number of particles found with orientations between 40° – 60°, which actually have an orientation of 0°. In the fluidized state, when the bed is in motion this problem did occur less strongly.

In Table 3 results from the analysis of the average particle height and orientation are given in terms of total number of detected particles and the average absolute deviation for all four particle types. Based on these results the quality of the automated script for the determination of particle orientations is found acceptable for all 4 analyzed particles types and therefore is used for the further study of the packed and fluidized bed in the following section.

4.2. Fluidization

In the following section mean pressure drops in experiments and corresponding coupled DEM–CFD simulations are outlined for 13 different particle shapes. All experiments and simulations have been repeated multiple times, the error bars show variations in terms of minimal and maximal values.

Results for $d_e = 7$ mm particles are displayed in Fig. 5. In Fig. 5a the results of the numerical and experimental examinations of spherical particles are shown. Good agreement between simulation and experiment can be observed for the fluidized range from U > 1.4 m/s onwards with an average deviation of $\overline{\Delta p} = 8$ Pa, for velocities U < 1.4 m/s there is a slightly bigger mean deviation of $\overline{\Delta p} = 48$ Pa. Our previous study [46] showed that for spherical particles the Ergun [39], Wen and Yu [66] model, which incorporates the Ergun equation for the calculation of the fixed bed gives better results. As it is less accurate for complex shaped particles this study was performed exclusively with the submodels for the drag force calculation by Hölzer and Sommerfeld [35] and Di Felice [36].

The outcome for ideal cylinders with the dimensions 6 mm × 6 mm is given in Fig. 5b. Good agreement between experiment and simulation can be seen over the entire velocity range, especially in the fixed bed regime with an average pressure drop difference of $\overline{\Delta p} = 15$ Pa. Multiple repetitions of the same experiment show a high repeatability with an average deviation of $\overline{\Delta p} = 13$ Pa.

The results for 5 mm × 6 mm × 6 mm cubes are displayed in Fig. 5c. It can be observed that for velocities below the fluidization point of $U_{mf} = 0.7$ m/s experiment and simulation are in a good agreement of $\overline{\Delta p} = 10$ Pa, though the experimental data shows high variations between different runs. This is the result of different initial bed structures with locally deviating porosities. As the tightest possible packing for cubes leaves no voids, these variations in the local porosity are stronger than for cylinders and sphere of comparable size. The variation between simulations and experiments increases once the minimum fluidization velocity is passed at $U_{mf} > 0.7$ m/s with $\overline{\Delta p} = 44$ Pa. This is the result of an incomplete fluidization in the experiments, as stacks of particles are not fully suspended but instead remain motionless in the corners of the vessel. With increasing superficial gas velocities more and more of these particles are released into the active region of the fluidized bed, so that the pressure drop increases. Opposite behavior can be observed for the simulations; at lower velocities all particles are suspended in the fluid being in motion and only at higher velocities particles attach to the walls and settle there. This behavior results in a decrease of the pressure drop with increasing superficial gas velocity.

The outcome for elongated cylinders with the dimensions 4 mm × 14 mm is displayed in Fig. 5d. A deviation between experiment and simulation can be observed for the fixed bed regime at $U_{mf} < 0.9$ m/s of $\overline{\Delta p} = 120$ Pa. At U = 1 m/s the values for both experiment and simulation approach each other and the average deviation decreases to $\overline{\Delta p} = 25$ Pa. Elongated particles like the 4 mm × 14 mm cylinders show the tendency to form channels, so that not the entire bed is in motion, but only particles within the channels. This is observed starting at the minimum fluidization velocity up to U = 1.6 m/s. The simulation does not reproduce this behavior as the fluid velocity is only represented through an averaged grid based velocity. Higher fluid velocities in the channels and lower velocities in the surrounding particle accumulations cannot be resolved, as the DEM–CFD grid is relatively coarse with cells bigger than a particle. Additionally, in the DEM static friction is not separately modeled for, which may affect how the interlocking between particles is represented.

In Fig. 5e the outcome for 4 mm × 4 mm × 11 mm elongated cuboids is given. Experiment and simulation are in good agreement for the entire velocity range with average deviations of $\overline{\Delta p} = 20$ Pa. Deviations between two runs of the same experiment are small with an average deviation of $\overline{\Delta p} = 23$ Pa. Similar to the elongated cylinders the elongated cuboids show channel flow following the minimum fluidization velocity. Full fluidization, where the entire bed is in motion and no more channels are observed, starts at U = 1.3 m/s. Again the simulation is not able to fully reproduce this effect; fluidization without channel flow starts once the highest pressure drop is reached at $U_{mf} = 0.8$ m/s.

Results for plates with the dimensions 2 mm × 9 mm × 10 mm are given in Fig. 5f. The fixed bed velocity range of U ≤ 0.6 m/s can be reproduced with high accuracy; the average deviation amounts to $\overline{\Delta p} = 10$ Pa. Similar to the elongated cuboids displayed in Fig. 5e, the 2 mm × 9 mm × 10 mm plates show channel flow behavior until the complete fluidization velocity is reached at U = 1.5 m/s. This channel flow is characterized by strong deviations between multiple repetitions of the same experiment, as the size and amount of the channels changes between every repetition. The simulation shows full fluidization and motion of all particles; the pressure drop corresponds to this and is obtained in the range of the maximum values of the experiment. Once the full fluidization is reached in the experiment, differences between simulation and experiment become lower with an average deviation of $\overline{\Delta p} = 30$ Pa.

Deviations between simulation and experiment can be observed in the results of the 2 mm × 6 mm × 15 mm elongated plates given in Fig. 5g. For the velocities analyzed in this study channel flow occurs. A state where every particle is in motion could not be reached, previous examinations showed that a velocity of U = 2.9 m/s is necessary for this [46]. Resulting from this channel flow are strong deviations between multiple repetitions of the same experiment of $\overline{\Delta p} = 100$ Pa. The simulation results lay at the upper range of the experiments from $U_{mf} > 0.9$ m/s onwards as generally more particles are suspended in the fluid.

Experimental and numerical results for the pressure drop for particles that are volume equivalent to a $d_p = 5$ mm sphere are outlined in Fig. 6. They are included to see if the column to particle diameter ratio D/d_e and thereby the resolution of the CFD-model do have an influence on the results.

Fig. 6a gives the results for 5 mm spheres, which are comparable in their behavior with the 7 mm spheres. At low gas velocities the pressure drop of the fixed bed is slightly underestimated by the simulations however the fluidized bed starting from $U_{mf} = 1$ m/s onwards is approximated with good accuracy. Note, that the deviation of the

Fig. 3. Particle height distributions for 4 different particle types in fixed and fluidized bed cases for (a) 4 mm × 14 mm elongated cylinders, (b) 4 mm × 4 mm × 11 mm elongated cuboids, (c) 5 mm × 6 mm × 6 mm cubes and (d) 6 mm × 6 mm ideal cylinders.
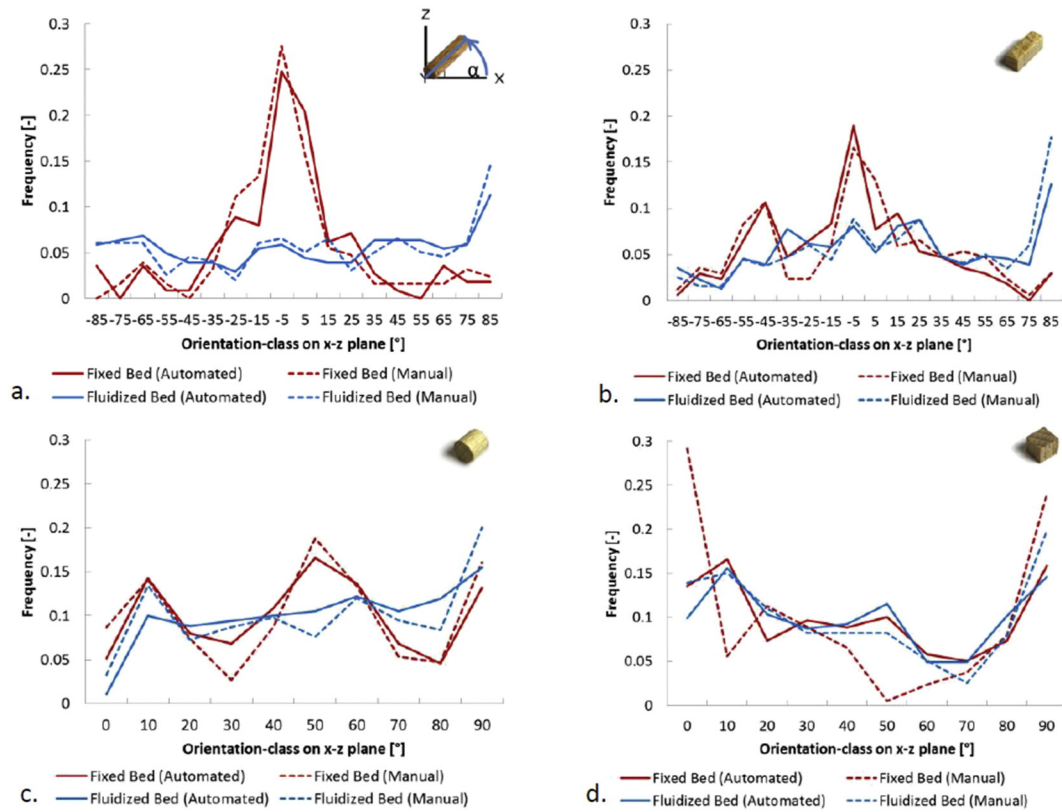
Fig. 4. Validation of the particle orientation derived with the automated method in Matlab compared to manual measurements done in Inkscape for (a) 4 mm × 14 mm elongated cylinders, (b) 4 mm × 4 mm × 11 mm elongated cubes, (c) 6 mm × 6 mm ideal cylinders and (d) 5 mm × 6 mm × 6 mm cubes.

pressure drop is not a result of a mismatch in porosity and/or bed height between simulations and experiments.

In Fig. 6b results for 4 mm × 4 mm × 4 mm cubes are given. Through equal dimensions in width, depth and height these cubes have the potential to form local structures with very low porosities. Very good agreement in the fixed bed can be observed up to the minimum fluidization velocity of $U_{mf} = 0.8$ m/s with an average deviation of $\overline{\Delta p} = 13$ Pa. The experimental results show an instant decline of the pressure drop afterwards. This decline is the result of the interlocking between the particles which is of a much greater magnitude for the cubes than for the spheres. This interlocking of particles has to be overcome before fluidization can take place. The results of the simulations show only a small decline of the pressure drop once the fixed bed regime is overcome. The simplified friction model included in the DEM used in this study could be one reason for this, as static friction is not separately modeled for. Additionally, the pressure drop declines in the simulations with increasing gas velocity, which indicates that particles

successively orientate with the walls; this tendency is not equally reported for in the experiments.

Results for elongated cuboids with the dimensions 3 mm × 3 mm × 7 mm are displayed in Fig. 6c. Fluidization in the DEM–CFD can be observed at a 0.2 m/s higher velocity than in the respective experiments, which already fluidize at $U_{mf} = 0.6$ m/s. The average deviation for the fixed bed amounts to $\Delta p = 120$ Pa, while the fluidized bed (U > 0.8 m/s) has an average deviation of $\Delta p = 18$ Pa. The difference in the pressure drop for the fluidized regime is the result of partial fluidization in the experiment as stacks of particles rest in the corners and at the walls of the vessel.

Results for plates with the dimensions 2 mm × 5 mm × 6 mm are displayed in Fig. 6d. These show similar behavior to the cubes discussed in Fig. 6b. The pressure drop of the fixed bed is approximated with high accuracy, while the pressure drop in the fluidized bed is overestimated at low velocities (U < 1.4 m/s). With an increasing gas velocity experiments and simulations are in good agreement. The average deviation

Table 3
Results of the image analysis validation including the total amount of detected frontwards/sidewards facing particles for manual and automated detection, the differences between both recognition methods, and the average absolute deviations of the frequency distribution of the particle height and of the particle orientation.

Particle Type	Bed state	# of front manual (FM)	# of front auto (FA)	FM–FA	# of side manual (SM)	# of side auto (SA)	SM–SA	$\Delta_{x,height}$ [−]	$\Delta_{x,orient}$ [−]
	Fixed	64	72	−8	104	88	16	0.015	0.019
4 × 14	Fluidized	36	68	−32	192	171	21	0.008	0.010
	Fixed	65	74	−9	175	175	0	0.010	0.016
4 × 4 × 11	Fluidized	60	70	−10	334	329	5	0.005	0.010
	Fixed	84	77	7	153	147	6	0.012	0.018
6 × 6	Fluidized	135	126	9	318	304	14	0.005	0.020
	Fixed	–	–	–	239	222	17	0.014	0.057
5 × 6 × 6	Fluidized	–	–	–	361	342	19	0.015	0.019
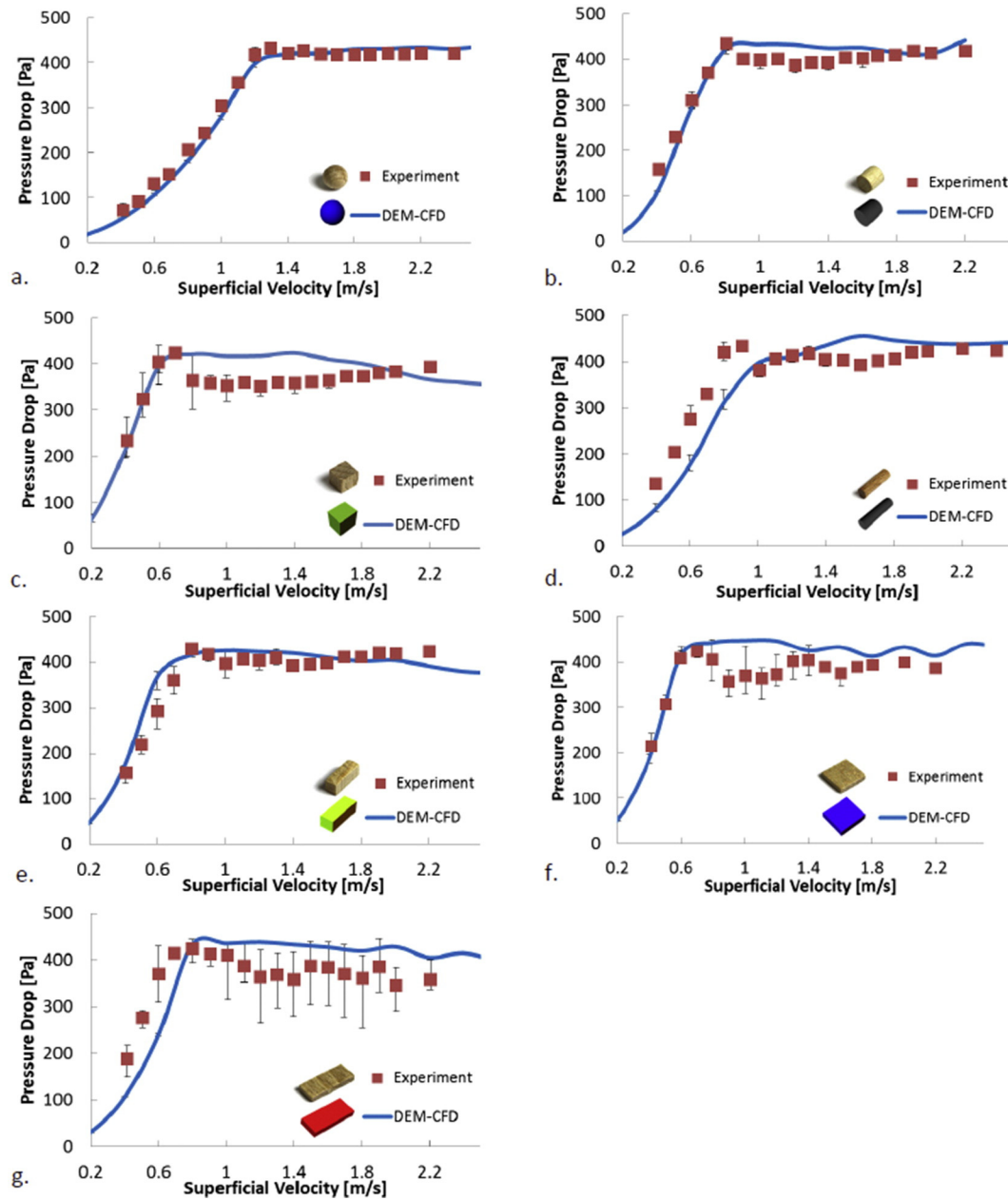
Fig. 5. Pressure drops of $d_e = 7$ mm class particles obtained for increasing superficial gas velocities in simulations and experiments for (a) 7 mm spheres, (b) 6 mm × 6 mm ideal cylinders, (c) 5 mm × 6 mm × 6 mm cubes, (d) 4 mm × 14 mm elongated cylinders, (e) 4 mm × 4 mm × 11 mm cuboids, (f) 2 mm × 9 mm × 10 mm plates and (g) 2 mm × 6 mm × 15 mm elongated plates.

of the pressure drop over the entire velocity range amounts to $\overline{\Delta p} = 35$ Pa.

The pressure drop behavior of elongated plates with the dimensions 2 mm × 4 mm × 8 mm is given in Fig. 6e. The minimum fluidization velocity is found to be 0.2 m/s higher in the DEM–CFD than the experiment. Differences in the pressure drop of the fixed bed regime amount to $\overline{\Delta p} = 40$ Pa. Partial fluidization in the experiment leads to an average deviation between experiment and the DEM–CFD of $\overline{\Delta p} = 40$ Pa for the fluidized bed regime (U > 0.8 m/s).

The last examined particle shape are elongated cuboids with the dimensions 2 mm × 3 mm × 11 mm for which the results are given in Fig. 6f. Similar to the elongated $d_e = 7$ mm plates (Fig. 5g) the experimental data shows a high variance between multiple repetitions, as channel flow occurs. The simulation of this particle type cannot predict

the minimum fluidization velocity correctly; instead a 0.2 m/s higher minimum fluidization velocity is reported. The pressure drop of the fixed bed range up to $U_{mf} < 0.6$ m/s lies bellow the experimentally determined values, with an average deviation of $\overline{\Delta p} = 140$ Pa. Partial fluidization leads to an overestimation of the pressure drop for the fluidized range from U > 0.8 m/s onwards, with an average deviation of $\overline{\Delta p} = 38$ Pa.

4.3. Orientation and particle height distributions

Besides a quantitative analysis of the pressure drop, an in detail look at particle heights and orientations is performed in this study to further analyze and validate the submodels [35,36] used for the drag force calculation of complex shaped particles in the DEM–CFD. These

submodels introduce parameters that are directly dependent on the orientation of a particle, namely the projection area perpendicular to the flow $A_\perp$ and the crosswise sphericity $\phi_\perp$. The average particle height, as a measure for the bed expansion, relates to the porosity ε_f of a fluidized bed. Experiments have been analyzed with the Matlab-script described in Section 2.2, while particle data from the DEM–CFD is readily available. For a better comparison between experimentally obtained data and DEM–CFD only particles visible in the simulations along the x-z pane of the vessel have been analyzed. Four different $d_e = 7$ mm particles including elongated cuboids and cylinders as well as ideal cylinders and cubes have been examined at four different velocities from 0 m/s to 2.4 m/s. To gain statistically relevant data up to 250,000 particles have been detected and analyzed per particle type and gas velocity in the fluidized states. For the fixed bed, only a single image is analyzed per series, as no change in the particle positions and orientations occurs over time.

The outcome of four different $d_e = 7$ mm particle shapes is given in Fig. 7, with the experimental results for elongated 4 mm × 14 mm cylinders shown in (a) and numerical results shown in (b). Error bars in the experimental results are obtained through the validation described in Section 4.1 as averaged absolute errors between manual and automatic analysis. As the determination of particle heights in the simulations is exact, no error bars are given. Good agreement between the experimental and numerical results can be observed for the fixed bed, with an average deviation in frequency of $\overline{\Delta_x} \approx 0.1$ for the lower, dense regions of the bed up to h = 10 cm. The maximum particle height of 11 cm is identical for both simulation and experiment. The

corresponding pressure drop (compare Fig. 5d) shows some deviation, which underlines the need to analyze not only the particle heights, but also the orientations. At a superficial velocity of U = 1.6 m/s the obtained pressure drop of the DEM–CFD reaches a local maximum of $\Delta p_{max} = 456$ Pa, while the experiments show the opposite behavior and reach a local minimum of $\Delta p_{min} = 392$ Pa (compare Fig. 5d). Corresponding differences can be found in the maximum average bed height; the experimental analysis shows the particle height maximum at h = 23 cm, while the particles in the DEM–CFD have their maximum at only h = 15 cm. For the velocities of 2.0 m/s and 2.4 m/s both the particle height distributions and the pressure drops match well between experiments and the DEM–CFD.

Results from the experiments of 4 mm × 4 mm × 11 mm elongated cuboids are given in Fig. 7c and numerical results in Fig. 7d. Good agreement between the experimental and numerical results for all four examined velocities can be observed, with an average absolute deviation of $\overline{\Delta_x} \approx 0.01$ for the fixed bed and between $\overline{\Delta_x} \approx 0.003 - 0.005$ for the fluidized cases. Fig. 7e and f show the experimental/numerical results for the particle height distribution for 5 mm × 6 mm × 6 mm cubes. Good agreement for the fixed bed can be observed, which reflects in the pressure drop which is also of good agreement (compare Fig. 5c). For the three fluidized states some deviation between experiment and simulation can be observed, the average particle height is up to two centimeters higher in the experiments.

The last particle type that is analyzed in regards to the bed height is the ideal 6 mm × 6 mm cylinder displayed in Fig. 7g (simulations) and Fig. 7h (experiments). The particle heights in the fixed bed are in good
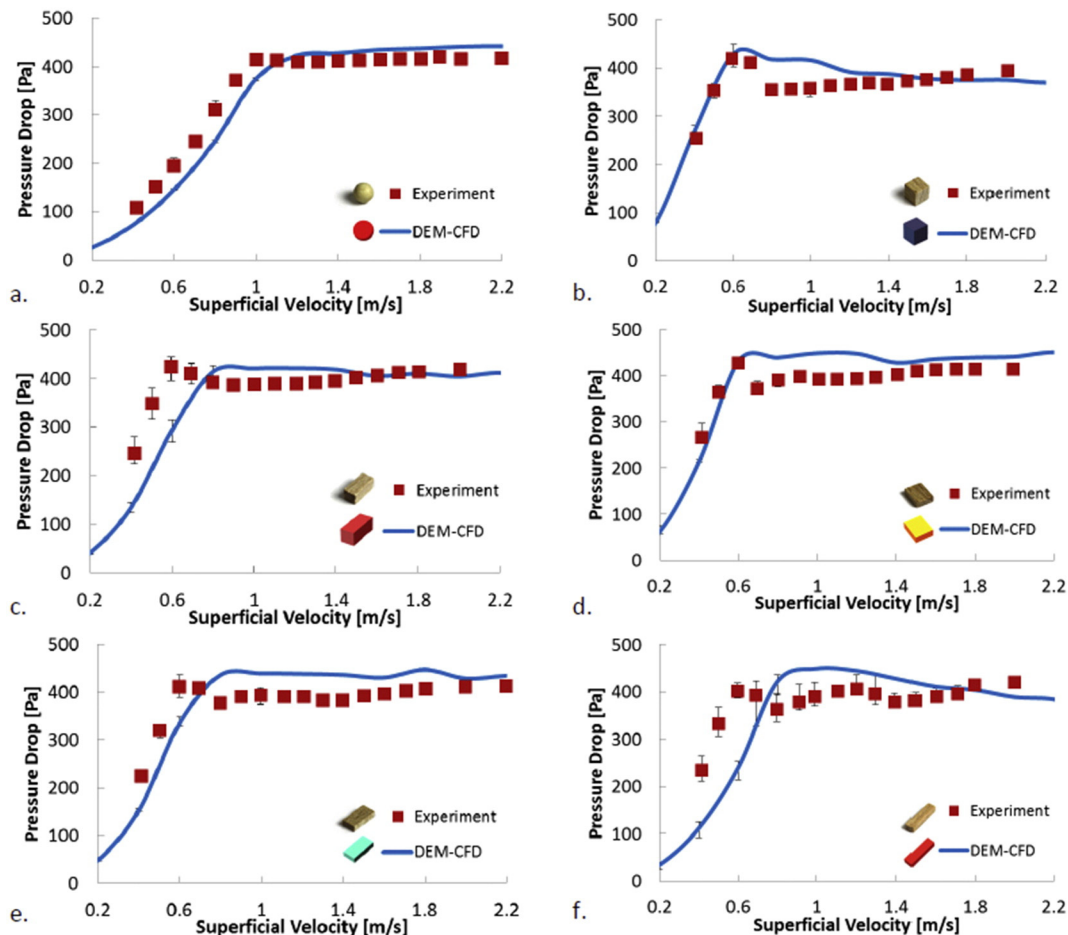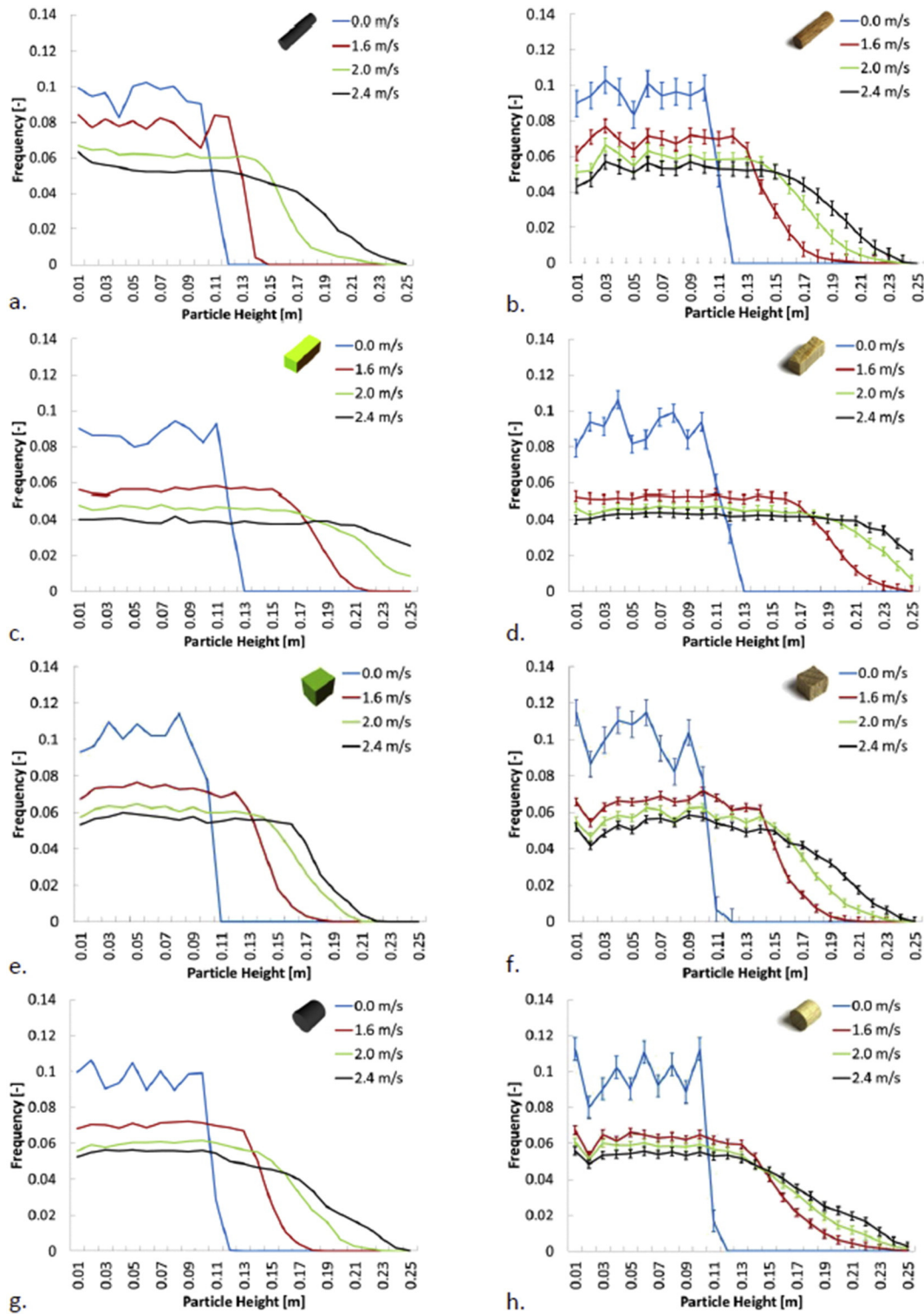

Fig. 6. Pressure drop of $d_e = 5$ mm class particles obtained for increasing superficial gas velocities in simulations and experiments for (a) 5 mm spheres, (b) 4 mm × 4 mm × 4 mm cubes, (c) 3 mm × 3 mm × 7 mm elongated cuboids, (d) 2 mm × 5 mm × 6 mm plates, (e) 2 mm × 4 mm × 8 mm elongated plates and (f) 2 mm × 3 mm × 11 mm elongated cuboids.
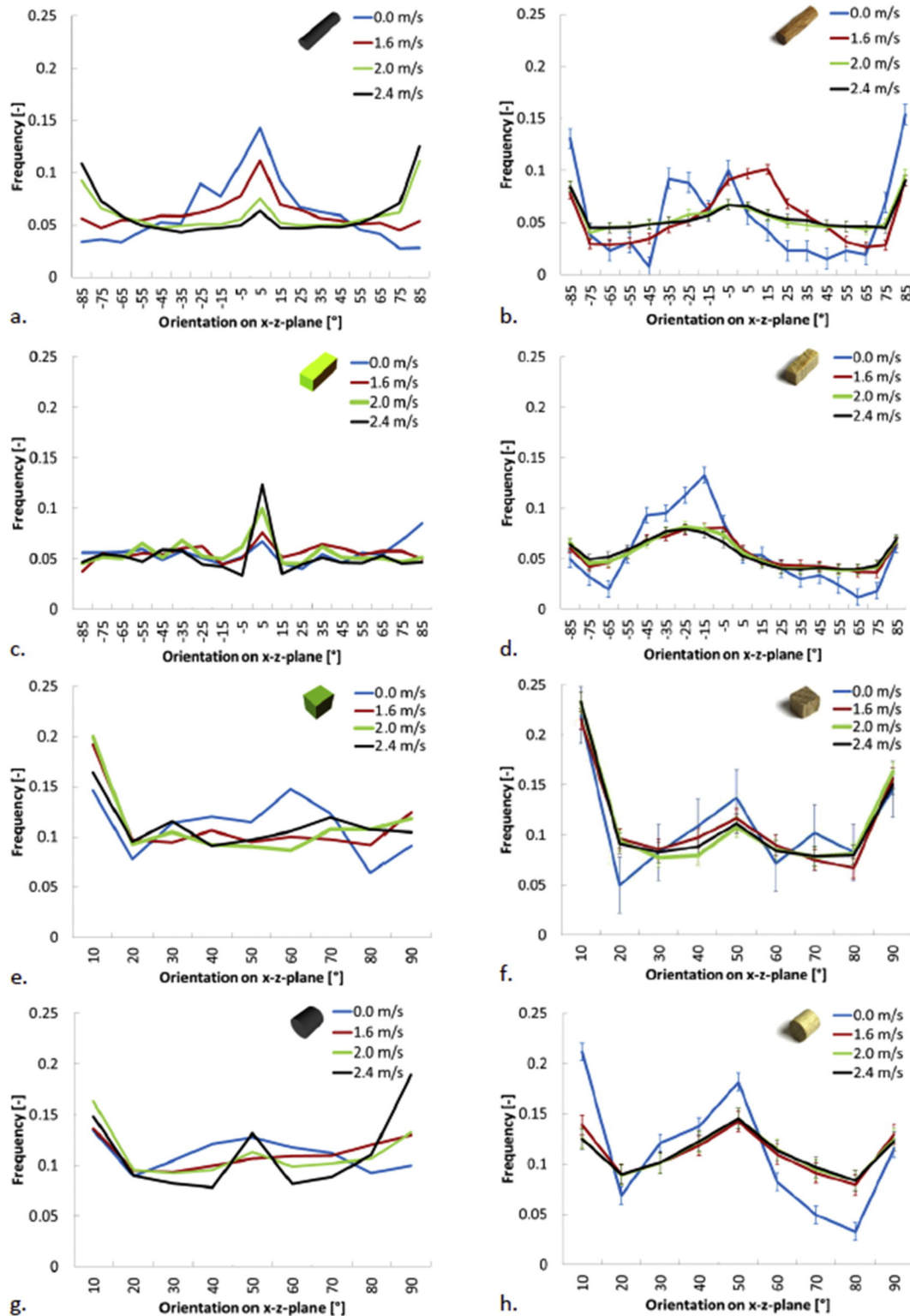
Fig. 7. Particle height distributions for 4 mm × 14 mm of simulations (left column) and experiments (right column) for elongated cuboids (a,b), 4 mm × 4 mm × 11 mm elongated cuboids (c,d), 5 mm × 6 mm × 6 mm cuboids (e,f) and 6 mm × 6 mm ideal cylinders (g,h).

agreement between the experiments and the DEM–CFD. Similarly, the pressure drop of the fixed bed region for $U_{mf} < 0.8$ m/s is in good agreement (compare Fig. 5b). Some deviation of the particle height occurs for $U = 1.6$ m/s, which amounts to $\overline{\Delta_x} \approx 0.007$ for the upper parts of the bed from h = 13 cm to 23 cm. Less deviation occurs for the velocities of U =

2.0 m/s and U = 2.4 m/s, so that the former is in good agreement and the latter is in very good agreement with the experimental data.

Particle orientation distributions for the four different particle geometries are given in Fig. 8 with numerical results in the left and experimental results being shown in the right column. Error bars in

Fig. 8. Frequency distribution of the orientation projected onto the x-z plane for simulations (left column) and experiments (right column) for (a,b) 4 mm × 14 mm elongated cylinders, (c,d) 4 mm × 4 mm × 11 mm elongated cuboids, (e,f) 5 mm × 6 mm × 6 mm cubes and (g,h) 6 mm × 6 mm ideal cylinders.

the experimental results express the average absolute deviation between the manual and automated evaluation. Orientations are calculated discretely for every particle in the DEM and are therefore exact so that no error bar is given. Orientations for 4 mm × 14 mm elongated cylinders are given in Fig. 8a and b in the range from −89° to 90°. Values

around 0° can be interpreted as a horizontal/lying particle while values close to −89° and 90° indicate vertical/standing particles. The fixed bed shows deviations for the angles that indicate vertical alignment, as these are the predominant occurring orientations in the experiments, but the least occurring in the simulations. These deviations can explain the

differences in the pressure drop of the velocity range associated with the fixed bed, which are present despite the good match of particle height distributions. With differences in the particle orientations local porosities might differ while the total porosity of the system remains unchanged. Local porosity variations can influence the pressure drop of a fixed bed system, which was examined in closer detail in our previous study [46].

With an increase of the superficial velocity the experimental and numerical results fit increasingly better to each other. For U = 1.6 m/s some deviations for the vertically orientated particles remain, while at U = 2.0 m/s und U = 2.4 m/s experiment and simulation are in good agreement. It can be observed in both the experiments and the simulations that with increasing superficial velocities particles orientate themselves more vertically, while the amount of horizontally aligned particles decreases. These results confirm the findings of Cai et al. [56], who examined wooden cylinders of various elongations experimentally and numerically through a Euler–Lagrange method in a fluidized bed and these of Ku and Lin [54], who examined the orientation of cylinders of different aspect ratios in a pipe flow with a direct numerical simulation using the Lattice Boltzmann method.

The findings for 4 mm × 4 mm × 11 mm elongated cuboids are given in Fig. 8c for the DEM–CFD and in Fig. 8d for the experiments. For the fixed bed some deviations can be observed between simulation and experiment, as the experimental results have a maximum for horizontal orientations, while the simulations are relatively evenly distributed with only a local maximum for the horizontal orientations. This explains the deviations found in the pressure drop of the fixed bed of the elongated cuboids displayed in Fig. 5e. In the fluidized state experimental results show only small variations between the orientation distributions for all three velocities, with small maxima at both horizontal and vertical orientations. Contrary to the 4 mm × 14 mm elongated cylinders, the elongated cuboids do not show an increase in the frequency of the vertical orientations with increasing superficial velocities as also reported in the literature [54–56]. This is in line with Cai et al. [56], who show that particles below a certain elongation ratio can be treated as equidimensional particles.

The DEM–CFD is able to reproduce this behavior; as analogous to the experiments elongated cylinders, which have a higher elongation ration than the elongated cuboids of this study, show a change of the orientation with increasing superficial velocities while elongated cuboids do not. Cuboids with the dimensions 5 mm × 6 mm × 6 mm are displayed in Fig. 8e and f. Simulation and experiment show only minor changes for increasing superficial gas velocities. Both methods have a maximum orientation at 0–10° while the other orientations occur equally often. An exception in the experiment can be found in the 90° class, which occurs more commonly. Differences in the pressure drop for this particle shape mostly originate from particles that are not fluidized, which can be found at lower superficial velocities in the experiments and higher superficial velocities in the simulations. At U = 2.0 m/s the pressure drop nearly becomes equal for both methods. Here the amount of unfluidized particles converges in the simulation and experiment, which mostly occurs in the corners of the vessel and can be observed visually in both setups.

In Fig. 8g and h the results for the orientation distributions of 6 mm × 6 mm ideal cylinders are displayed. Variations between simulations with different superficial gas velocities are small, and with increasing superficial gas velocities the orientations become more evenly distributed. Similarly the experimental data remains mostly unchanged between different gas superficial velocities. The distribution generally has maxima in the 0, 50 and 90 degree classes. 50° correspond to the maximum projection area of the particle. The results of the simulations are mostly in agreement with this; only at U = 1.6 m/s no maximum can be observed in the 50° class. These slight differences in the orientations agree with the results found in the examination of the pressure drop (compare Fig. 5c), which also shows minor variations between both methods.

5. Conclusions

Pressure drops of 13 differently shaped Geldart-D particle groups have been examined in a laboratory scale fluidized bed, both experimentally and numerically. A combined DEM–CFD approach which considers particle shapes and orientations in the drag force model was used in the simulation. A PTV-Matlab script was developed to determine particle orientations and heights in the experiments, which was validated and then used to compare experiments and simulations. The following conclusions can be drawn from this study:

- The analysis of the pressure drops of different particles shapes and sizes shows that DEM–CFD simulations are a useful tool in the description of fluidized systems as the results are in good agreement with the corresponding experiments for most particle types. Minimum fluidization velocities were accurately described by the DEM–CFD except for some particle types that differ strongly from the spherical shape.
- Particles with a low sphericity show tendencies to form channels at low superficial velocities. These channels result in a lower pressure drop as not all particles are fully suspended. The DEM–CFD cannot describe this behavior. An extension of the DEM code to more detailedly include static friction and a resolved study of the interlocking through higher resolution simulation methods like FEM-DEM can be the next steps to gain a better understanding.
- Limitations of the DEM–CFD exist when particles reach high elongations, as the grid size has to be above the particle size. Wall effects and flow structures inside the vessel, like channel flow cannot adequately be reproduced on a coarse grid. A coupling of the DEM with a particle resolved flow simulation like the Lattice Boltzmann Method can be utilized to further study and characterize flow phenomena inside fluidized beds.
- Stacks of particles can accumulate in the corners of the fluidized bed especially for non-spherical equidimensional particles like cubes and ideal cylinders. The amount of these particles differs between simulation and experiment and result in differences in the pressure drop.
- The particle height distributions are in good agreement for the majority of the analyzed particles and superficial velocities. In case of differences between both methods, the simulations generally showed a lower average height. The influence of extended particle/fluid force models that account for further forces like the Magnus force or the Basset force could be analyzed in this context.
- The analysis of the particle orientations showed the strong influence orientations have on the pressure drop of the examined systems. Differences in the pressure drop of fixed beds at equal bed heights and therefore integral porosities can be explained through different orientation distributions between experiments and simulations and therefore varying local porosities.
- Elongated cylinders show a tendency to align themselves with the flow with increasing superficial velocities, which confirms the findings by Ku and Lin [54] and Zhang et al. [55]. Equidimensional particles showed no such behavior and orientations stayed mostly constant with increasing superficial velocities. Elongated cuboids with a smaller elongation ratio than the elongated cylinders showed orientation distributions which are more comparable to equidimensional particles. This behavior was correctly reproduced by the DEM–CFD.

of Scholars and Other Researchers and the Promotion of Student Research (VP1-3.1-ŠMM-01) of the Program of Human Resources.

Nomenclature

$A_\perp$	cross-sectional area perpendicular to the flow	[m^2]
C_D	drag coefficient	[−]
D	column diameter	[m]
d_e	equivalent surface sphere diameter $d_e = (\frac{6}{\pi} V_p)^{1/3}$	[m]
d_p	particle diameter	[m]
e^n	coefficient of restitution	[−]
F	force vector	[N]
$\vec{f}_{int}$	volumetric particle/fluid interaction momentum source	[N/m^3]
g	gravitational acceleration	[m/s^2]
h	height	[m]
I	inertia tensor	[kg·m^2]
k	spring stiffness	[N/m]
L	bed height	[m]
M	external moment	[Nm]
m	mass	[kg]
n	normal vector	[−]
p	pressure	[N/m^2]
Re	particle Reynolds number $\text{Re} = \frac{\varepsilon_f \rho_f d_e |\vec{u}_f - \vec{v}_i|}{\eta_f}$	[−]
R_s	specific gas constant air	[J/(kg·K)]
T	temperature	[K]
t	tangential unit vector	[−]
U	superficial gas velocity	[m/s]
$\vec{u}$	physical velocity vector	[m/s]
V	volume	[m^3]
v	fluid cell average particle velocity	[m/s]
$\vec{v}_{rel}^n$	normal velocity	[m/s]
W	angular velocity	[rad/s]
x	exact value (manually determined)	[−]
$x\sim$	approximated value (automatically determined)	[−]
$\vec{x}$	position vector	[m]

Greek symbols

β	fluid cell average particle/fluid friction coefficient	[kg/(m^3·s)]
γ^n	damping coefficient	[kg/s]
Δ_x	average absolute error $\Delta_x = \frac{1}{I} \sum (|x_i - x\sim_i|)$	[−]
δ	overlap during contact	[m]
δ_x	average relative error $\delta_x = \frac{1}{I} \sum (\frac{|x_i - x\sim_i|}{x_i})$	[−]
ε	porosity	[−]
η	dynamic viscosity	[kg/(m·s)]
Λ	rotation matrix	[−]
μ_c	friction coefficient	[−]
ξ	relative tangential displacement	[m]
ρ	density	[kg/m^3]
τ	viscous stress tensor	[N/m^2]
ϕ	sphericity $\phi = (36\pi \cdot V_p^2 / A_p^3)^{\frac{1}{3}}$	[−]
$\phi_\perp$	crosswise sphericity	[−]
χ	correction factor	[−]

Subscripts

A	ambient
f	fluid
fb	fixed bed
i	index
mf	minimum fluidization velocity
p	particle
pp	particle/particle
pw	particle/wall
t	total

Superscripts

c	contact
d	drag
n	normal
pf	particle/fluid
t	tangential
∇p	pressure
	gradient

References

[1] P. Basu, Combustion of coal in circulating fluidized-bed boilers: a review, Chem. Eng. Sci. 54 (1999) 5547–5557, http://dx.doi.org/10.1016/S0009-2509(99)00285-7.

[2] C.A.M. da Silva, J.J. Butzge, M. Nitz, O.P. Taranto, Monitoring and control of coating and granulation processes in fluidized beds — a review, Adv. Powder Technol. 25 (2014) 195–210, http://dx.doi.org/10.1016/j.apt.2013.04.008.

[3] M. Rüdisüli, T.J. Schildhauer, S.M.A. Biollaz, J.R. van Ommen, Scale-up of bubbling fluidized bed reactors — a review, Powder Technol. 217 (2012) 21–38, http://dx.doi.org/10.1016/j.powtec.2011.10.004.

[4] B. Leckner, P. Szentannai, F. Winter, Scale-up of fluidized-bed combustion — a review, Fuel 90 (2011) 2951–2964, http://dx.doi.org/10.1016/j.fuel.2011.04.038.

[5] T. Hagemeier, M. Börner, A. Bück, E. Tsotsas, A comparative study on optical techniques for the estimation of granular flow velocities, Chem. Eng. Sci. 131 (2015) 63–75, http://dx.doi.org/10.1016/j.ces.2015.03.045.

[6] K.A. Buist, A.C. van der Gaag, N.G. Deen, J.A.M. Kuipers, Improved magnetic particle tracking technique in dense gas fluidized beds, AICHE J. 60 (2014) 3133–3142, http://dx.doi.org/10.1002/aic.14512.

[7] H. Kruggel-Emden, S. Wirtz, Analysis of residence time distributions of different solid biomass fuels by using radio frequency identification (RFID), Energy Technol. 2 (2014) 498–505, http://dx.doi.org/10.1002/ente.201300170.

[8] B.P.B. Hoomans, J.A.M. Kuipers, W.J. Briels, W.P.M. van Swaaij, Discrete particle simulation of bubble and slug formation in a two-dimensional gas-fluidised bed: a hard-sphere approach, Chem. Eng. Sci. 51 (1996) 99–118, http://dx.doi.org/10.1016/0009-2509(95)00271-5.

[9] K.D. Kafui, C. Thornton, M.J. Adams, Discrete particle-continuum fluid modelling of gas–solid fluidised beds, Chem. Eng. Sci. 57 (2002) 2395–2410, http://dx.doi.org/10.1016/S0009-2509(02)00140-9.

[10] Y.Q. Feng, B.H. Xu, S.J. Zhang, A.B. Yu, P. Zulli, Discrete particle simulation of gas fluidization of particle mixtures, AICHE J. 50 (2004) 1713–1728, http://dx.doi.org/10.1002/aic.10169.

[11] R. Beetstra, M.A. van der Hoef, J.A.M. Kuipers, Numerical study of segregation using a new drag force correlation for polydisperse systems derived from lattice-Boltzmann simulations, Chem. Eng. Sci. 62 (2007) 246–255, http://dx.doi.org/10.1016/j.ces.2006.08.054.

[12] L.W. Rong, J.M. Zhan, Improved DEM–CFD model and validation: a conical-base spouted bed simulation study, J. Hydrodyn. 22 (2010) 351–359, http://dx.doi.org/10.1016/S1001-6058(09)60064-0.

[13] A.A. Munjiza, E.E. Knight, E. Rougier, Computational Mechanics of Discontinua, John Wiley & Sons, Ltd., Chichester, UK, 2011http://dx.doi.org/10.1002/9781119971160.

[14] P.A. Cundall, O.D.L. Strack, A discrete numerical model for granular assemblies, Géotechnique 29 (1979) 47–65.

[15] Y. Tsuji, T. Kawaguchi, T. Tanaka, Discrete particle simulation of two-dimensional fluidized bed, Powder Technol. 77 (1993) 79–87, http://dx.doi.org/10.1016/0032-5910(93)85010-7.

[16] T. Tsuji, K. Yabumoto, T. Tanaka, Spontaneous structures in three-dimensional bubbling gas-fluidized bed by parallel DEM–CFD coupling simulation, Powder Technol. 184 (2008) 132–140, http://dx.doi.org/10.1016/j.powtec.2007.11.042.

[17] H. Zhu, Z. Zhou, R. Yang, A.B. Yu, Discrete particle simulation of particulate systems: theoretical developments, Chem. Eng. Sci. 62 (2007) 3378–3396, http://dx.doi.org/10.1016/j.ces.2006.12.089.

[18] H.P. Zhu, Z.Y. Zhou, R.Y. Yang, A.B. Yu, Discrete particle simulation of particulate systems: a review of major applications and findings, Chem. Eng. Sci. 63 (2008) 5728–5770, http://dx.doi.org/10.1016/j.ces.2008.08.006.

[19] H. Wiinikka, R. Gebart, The influence of air distribution rate on particle emissions in fixed bed combustion of biomass, Combust. Sci. Technol. 177 (2005) 1747–1766, http://dx.doi.org/10.1080/00102200590959468.

[20] P. Perré, Multiscale modeling of drying as a powerful extension of the macroscopic approach: application to solid wood and biomass processing, Dry. Technol. 28 (2010) 944–959, http://dx.doi.org/10.1080/07373937.2010.497079.

[21] B.U. Kozanoglu, J. Welti Chanes, D. García Cuautle, J.P. Santos Jean, Hydrodynamics of large particle fluidization in reduced pressure operations: an experimental study, Powder Technol. 125 (2002) 55–60, http://dx.doi.org/10.1016/S0032-5910(01)00524-1.

[22] X. Qian, Y. Yan, Flow measurement of biomass and blended biomass fuels in pneumatic conveying pipelines using electrostatic sensor-arrays, IEEE Trans. Instrum. Meas. 61 (2012) 1343–1352, http://dx.doi.org/10.1109/TIM.2011.2175034.

[23] J.-P. Latham, a. Munjiza, The modelling of particle systems with real shapes, Philos. Transact. A Math. Phys. Eng. Sci. 362 (2004) 1953–1972, http://dx.doi.org/10.1098/rsta.2004.1425.

[24] K. Richards, M. Bithell, M. Dove, R. Hodge, Discrete-element modelling : methods and applications in the environmental sciences, Philos. Trans. R. Soc. Phys. Eng. Sci. 362 (2004) 1797–1816.

[25] I. Kock, K. Huhn, Influence of particle shape on the frictional strength of sediments — a numerical case study, Sediment. Geol. 196 (2007) 217–233, http://dx.doi.org/10.1016/j.sedgeo.2006.07.011.

[26] D. Höhner, S. Wirtz, H. Kruggel-Emden, V. Scherer, Comparison of the multi-sphere and polyhedral approach to simulate non-spherical particles within the discrete element method: influence on temporal force evolution for multiple contacts, Powder Technol. 208 (2011) 643–656, http://dx.doi.org/10.1016/j.powtec.2011.01.003.

[27] Y. Guo, J.S. Curtis, Discrete element method simulations for complex granular flows, Annu. Rev. Fluid Mech. 47 (2014) 21–46, http://dx.doi.org/10.1146/annurev-fluid-010814-014644.

[28] G. Lu, J.R. Third, C.R. Müller, Discrete element models for non-spherical particle systems: from theoretical developments to applications, Chem. Eng. Sci. 127 (2015) 425–465, http://dx.doi.org/10.1016/j.ces.2014.11.050.

[29] R. Caulkin, W. Tian, M. Pasha, A. Hassanpour, X. Jia, Impact of shape representation schemes used in discrete element modelling of particle packing, Comput. Chem. Eng. 76 (2015) 160–169, http://dx.doi.org/10.1016/j.compchemeng.2015.02.015.

[30] H. Kruggel-Emden, S. Rickelt, S. Wirtz, V. Scherer, A study on the validity of the multi-sphere discrete element method, Powder Technol. 188 (2008) 153–165, http://dx.doi.org/10.1016/j.powtec.2008.04.037.

[31] J.P. Latham, A. Munjiza, X. Garcia, J. Xiang, R. Guises, Three-dimensional particle shape acquisition and use of shape library for DEM and FEM/DEM simulation, Miner. Eng. 21 (2008) 797–805, http://dx.doi.org/10.1016/j.mineng.2008.05.015.

[32] K.C. Williams, W. Chen, S. Weeger, T.J. Donohue, Particle shape characterisation and its application to discrete element modelling, Particuology 12 (2014) 80–89, http://dx.doi.org/10.1016/j.partic.2013.02.014.

[33] W.-Q. Zhong, Y. Zhang, B.-S. Jin, M.-Y. Zhang, Discrete element method simulation of cylinder-shaped particle flow in a gas–solid fluidized bed, Chem. Eng. Technol. 32 (2009) 386–391, http://dx.doi.org/10.1002/ceat.200800516.

[34] S. Tran-Cong, M. Gay, E.E. Michaelides, Drag coefficients of irregularly shaped particles, Powder Technol. 139 (2004) 21–32, http://dx.doi.org/10.1016/j.powtec.2003.10.002.

[35] A. Hölzer, M. Sommerfeld, New simple correlation formula for the drag coefficient of non-spherical particles, Powder Technol. 184 (2008) 361–365, http://dx.doi.org/10.1016/j.powtec.2007.08.021.

[36] R. Di Felice, The voidage function for fluid-particle interaction systems, Int. J. Multiphase Flow 20 (1994) 153–159, http://dx.doi.org/10.1016/0301-9322(94)90011-6.

[37] J.E. Hilton, L.R. Mason, P.W. Cleary, Dynamics of gas–solid fluidised beds with non-spherical particle geometry, Chem. Eng. Sci. 65 (2010) 1584–1596, http://dx.doi.org/10.1016/j.ces.2009.10.028.

[38] L.W. Rong, K.J. Dong, A.B. Yu, Lattice-Boltzmann simulation of fluid flow through packed beds of uniform spheres: effect of porosity, Chem. Eng. Sci. 99 (2013) 44–58, http://dx.doi.org/10.1016/j.ces.2013.05.036.

[39] S. Ergun, Fluid flow through packed columns, Chem. Eng. Sci. 48 (1952) 89–94.

[40] Z.Y. Zhou, D. Pinson, R.P. Zou, A.B. Yu, Discrete particle simulation of gas fluidization of ellipsoidal particles, Chem. Eng. Sci. 66 (2011) 6128–6145, http://dx.doi.org/10.1016/j.ces.2011.08.041.

[41] B. Ren, W. Zhong, Y. Chen, X. Chen, B. Jin, Z. Yuan, et al., CFD–DEM simulation of spouting of corn-shaped particles, Particuology 10 (2012) 562–572, http://dx.doi.org/10.1016/j.partic.2012.03.011.

[42] B. Ren, W. Zhong, B. Jin, Y. Shao, Z. Yuan, Numerical simulation on the mixing behavior of corn-shaped particles in a spouted bed, Powder Technol. 234 (2013) 58–66, http://dx.doi.org/10.1016/j.powtec.2012.09.024.

[43] T. Oschmann, J. Hold, H. Kruggel-Emden, Numerical investigation of mixing and orientation of non-spherical particles in a model type fluidized bed, Powder Technol. 258 (2014) 304–323, http://dx.doi.org/10.1016/j.powtec.2014.03.046.

[44] J.E. Hilton, P.W. Cleary, The influence of particle shape on flow modes in pneumatic conveying, Chem. Eng. Sci. 66 (2011) 231–240, http://dx.doi.org/10.1016/j.ces.2010.09.034.

[45] H. Kruggel-Emden, T. Oschmann, Numerical study of rope formation and dispersion of non-spherical particles during pneumatic conveying in a pipe bend, Powder Technol. 268 (2014) 219–236, http://dx.doi.org/10.1016/j.powtec.2014.08.033.

[46] K. Vollmari, T. Oschmann, S. Wirtz, H. Kruggel-Emden, Pressure drop investigations in packings of arbitrary shaped particles, Powder Technol. 271 (2015) 109–124, http://dx.doi.org/10.1016/j.powtec.2014.11.001.

[47] G. Mohs, O. Gryczka, S. Heinrich, L. Mörl, Magnetic monitoring of a single particle in a prismatic spouted bed, Chem. Eng. Sci. 64 (2009) 4811–4825, http://dx.doi.org/10.1016/j.ces.2009.08.025.

[48] C. Penny, D. Rosero, D. Naylor, J. Friedman, Heat transfer to flat strips immersed in a fluidized bed, J. Heat Transf. 133 (2011) 071703, http://dx.doi.org/10.1115/1.4003530.

[49] M. Asif, Flow dynamic characterization of cylindrical particles, Part. Part. Syst. Charact. 26 (2009) 210–219, http://dx.doi.org/10.1002/ppsc.200700025.

[50] A. Busciglio, G. Vella, E. Mangano, G. Micale, R. Lucio, Digital image analysis technique for mixing pattern measurements in bi-dispersed 2D gas fluidized beds, Chem. Eng. Trans. 24 (2011) (http://onlinelibrary.wiley.com/doi/10.1002/cbdv.200490137/abstract (accessed January 28, 2013)).

[51] O.O. Olaofe, K.A. Buist, N.G. Deen, M.A. van der Hoef, J.A.M. Kuipers, Improved digital image analysis technique for the evaluation of segregation in pseudo-2D beds, Powder Technol. 244 (2013) 61–74, http://dx.doi.org/10.1016/j.powtec.2013.03.051.

[52] A.I. Kartushinsky, Y.A. Rudi, S.V. Tisler, M.T. Hussainov, I.N. Shcheglov, Application of particle tracking velocimetry for studying the dispersion of particles in a turbulent gas flow, High Temp. 50 (2012) 381–390, http://dx.doi.org/10.1134/S0018151X12030133.

[53] K.B. Zitoun, S.K. Sastry, Y. Guezennec, Investigation of three dimensional interstitial velocity, solids motion, and orientation in solid–liquid flow using particle tracking velocimetry, Int. J. Multiphase Flow 27 (2001) 1397–1414, http://dx.doi.org/10.1016/S0301-9322(01)00011-8.

[54] L. Ku, Motion and orientation of cylindrical and cubic particles in pipe flow, J. Zhejiang Univ. (Sci.) 9 (2008) 664–671.

[55] L.X. Zhang, J.Z. Lin, T.L. Chan, Orientation distribution of cylindrical particles suspended in a turbulent pipe flow, Phys. Fluids 17 (2005) 1–8, http://dx.doi.org/10.1063/1.2046713.

[56] J. Cai, Q. Li, Z. Yuan, Orientation of cylindrical particles in gas–solid circulating fluidized bed, Particuology 10 (2012) 89–96, http://dx.doi.org/10.1016/j.partic.2011.03.012.

[57] H. Kruggel-Emden, E. Simsek, S. Rickelt, S. Wirtz, V. Scherer, Review and extension of normal force models for the discrete element method, Powder Technol. 171 (2007) 157–173, http://dx.doi.org/10.1016/j.powtec.2006.10.004.

[58] H. Kruggel-Emden, S. Wirtz, V. Scherer, An analytical solution of different configurations of the linear viscoelastic normal and frictional–elastic tangential contact model, Chem. Eng. Sci. 62 (2007) 6914–6926, http://dx.doi.org/10.1016/j.ces.2007.08.049.

[59] R.C. Gonzalez, R.E. Woods, S.L. Eddins, Digital Image Processing Using MATLAB, McGraw-Hill Education, 2011.

[60] J. Canny, A computational approach to edge detection, IEEE Trans. Pattern Anal. Mach. Intell. PAMI-8 (1986)http://dx.doi.org/10.1109/TPAMI.1986.4767851.

[61] M.B. Dillencourt, H. Samet, M. Tamminen, A general-approach to connected-component labeling for arbitrary image representations, J. ACM 39 (1993) 253–280.

[62] P.V.C. Hough, Method and Means for Recognizing Complex Patterns, United States Pat. Off. US3069654 (1962).

[63] J. Hold, Charakterisierung der Mischungs- und Segregations- vorgänge in Modellwirbelschichten mit mono- und bidispersen sphärischen Partikelsystemen: Experimente und gekoppelte CFD/DEM-Modellierung(PhD-thesis, Bochum) 2013.

[64] H. Kruggel-Emden, F. Stepanek, A. Munjiza, A study on adjusted contact force laws for accelerated large scale discrete element simulations, Particuology 8 (2010) 161–175, http://dx.doi.org/10.1016/j.partic.2009.07.006.

[65] T. Bah, Inkscape: Guide to a Vector Drawing Program, 4th edition Prentice Hall, Boston, MA, US, 2011 (4 edition (May 16, 2011)).

[66] C.Y. Wen, Y.H. Yu, A generalized method for predicting the minimum fluidization velocity, AICHE J. 12 (1966) 610–612, http://dx.doi.org/10.1002/aic.690120343.